DIAGNOSTICS OF THE SMOS RADIOMETER ANTENNA SYSTEM AT THE DTU-ESA SPHERICAL NEAR-FIELD ANTENNA TEST FACILITY

C. Cappellin[1-2], A. Frandsen[1], S. Pivnenko[2], G. Lemanczyk[3], O. Breinbjerg[2]

[1]TICRA, Læderstræde 34, DK-1201, Copenhagen, Denmark
[2]Ørsted·DTU, Technical University of Denmark, DK-2800 Kgs. Lyngby, Denmark
[3]European Space Research and Technology Centre, Noordwijk, The Netherlands

Keywords: Antenna diagnostics, spherical near-field measurements, radiometer antenna, plane wave expansion, spherical wave expansion.

Abstract

The recently developed Spherical Wave Expansion-to-Plane Wave Expansion (SWE-to-PWE) antenna diagnostics technique is employed in an investigation of the antenna system in the Microwave Imaging Radiometer using Aperture Synthesis (MIRAS) for ESA's Soil Moisture and Ocean Salinity (SMOS) mission. The SWE-to-PWE antenna diagnostics technique successfully identifies the sources of the anomalies detected in 2 of the 138 MIRAS antenna far-field patterns that were measured during the on-ground calibration at the DTU-ESA Spherical Near-Field Antenna Test Facility in 2006. In addition to its obvious value for the SMOS mission, this investigation also provides an experimental validation of the SWE-to-PWE antenna diagnostics technique.

1 Introduction

The SMOS mission, scheduled for launch in 2008, is the latest Earth Observation Mission of the European Space Agency (ESA) [5]. Its purpose is to monitor the water cycle, the density of the seawater and the currents in the oceans to improve the knowledge of these phenomena and hence provide better weather and climate forecasts. A special radiometer, MIRAS, has been developed to capture the microwave radiation emitted from soil and ocean in the frequency band from 1.404 GHz to 1.423 GHz (L-band). In order to achieve the required spatial resolution, the radiometer consists of 69 independent dual-polarized receivers positioned on an 8 meter diameter Y-shaped support structure, that is folded during launch and un-folded once the satellite is in orbit. Each receiver includes a dual linearly polarized circular patch antenna.

For the purpose of accurately determining the soil moisture and ocean salinity, the radiometric signal processing requires an extremely accurate measurement of the receivers' antenna far-field patterns. A 1σ accuracy of 0.05 dB for the amplitude and 0.33° for the phase in a 70° angular region centred on the main beam direction was requested. The DTU-ESA Spherical Near-Field Antenna Test Facility at the Technical University of Denmark (DTU) [6] was selected to conduct the on-ground calibration of the MIRAS antenna patterns. After an investigatory study to improve measurement procedures and the measurement system during 2003 to 2005 [7]-[8], the final on-ground calibration measurements took place from November 2005 to July 2006, while the processing of the raw measurement data to determine the antenna far-field patterns was carried out in the fall of 2006.

During the last measurement series of the MIRAS, see Fig. 1, anomalies were detected in the antenna patterns of two MIRAS receivers.

Figure 1. Central part of the MIRAS, consisting of the hub and the three inner arm segments, on the tower of the DTU-ESA Spherical Near-Field Antenna Test Facility during the last measurement series.

In order to identify the source of these far-field anomalies a diagnostics of the two elements was performed based on the SWE-to-PWE antenna diagnostics technique [1]-[2]. The technique uses spherical near-field measurement data to compute the aperture field on a plane located in the extreme near-field of the antenna under test, and provides a spatial

resolution that may, in principle, exceed the traditional limit of half a wavelength. The aperture plane was chosen to be positioned on the outside surface of the Kapton-Germanium protection layer which covers the complete MIRAS structure, see Fig. 1.

The purpose of this work is, besides being an important step in the MIRAS on-ground calibration, to provide an experimental validation of the SWE-to-PWE antenna diagnostics technique, when working in the presence of noise, finite dynamic range, and other non-ideal phenomena typical of practical measurements.

The paper is organized as follows: in section 2 a summary of the SWE-to-PWE technique is provided, while in section 3 the two faulty elements are analyzed. Both the measured far-field patterns and the computed aperture field distributions will be shown for each of the two test cases, arriving at the identification of the antenna errors. All results are expressed in the S.I. rationalized system with the $e^{-i\omega t}$ time convention.

2 The SWE-to-PWE antenna diagnostics technique

Electrical and mechanical errors in an antenna may seriously affect the antenna performance, and while their presence is normally detected by anomalies in the measured far-field pattern, often only an analysis of the extreme near-field can facilitate the identification of those errors. However, the computation of the extreme near-field is generally not possible when the field is expressed as a SWE obtained from a spherical near-field measurement since the SWE is valid only outside the antenna minimum sphere of radius r_o, with r_o being the largest r-coordinate of the source. One way to overcome this limitation is to transform the SWE into the PWE which is valid on any z-plane $z > z_o$, with z_o being the largest z-coordinate of the source, see Fig. 2. Note that $|z_o| \le r_o$. Once the PWE is known, the extreme near-field can be computed by use of the Fourier transform and then subjected to diagnostics.

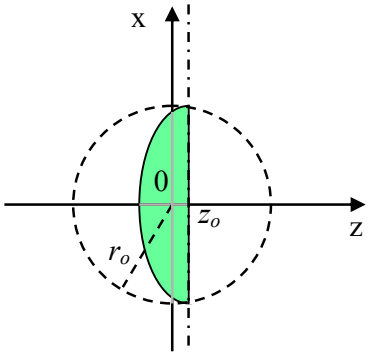

Figure 2. Spatial domains of validity of the SWE and PWE for a general antenna: the PWE is valid for $z > z_o$, the SWE for $r > r_o$.

To summarize the theory behind the SWE-to-PWE technique, we start by introducing the SWE of the electric field $\bar{E}$ radiated by an antenna circumscribed by a minimum sphere of radius r_o, [3],

$$\bar{E}(\bar{r}) = \frac{k}{\sqrt{\eta}} \sum_{n=1}^{\infty} \sum_{m=-n}^{n} Q_{1mn}^{(3)} \bar{F}_{1mn}^{(3)}(\bar{r}) + Q_{2mn}^{(3)} \bar{F}_{2mn}^{(3)}(\bar{r}), \quad r > r_o \tag{1}$$

where $Q_{1mn}^{(3)}$ and $Q_{2mn}^{(3)}$ are the expansion coefficients and $\bar{F}_{1mn}^{(3)}(\bar{r})$ and $\bar{F}_{2mn}^{(3)}(\bar{r})$ are the power-normalized spherical vector wave functions. The medium intrinsic admittance is η, k is the wave number, and $\bar{r}$ is the position vector expressed in terms of spherical coordinates (r, θ, φ) or rectangular coordinates (x, y, z). In practice, the n-summation of the SWE is typically truncated at $N = kr_o+10$ since this is sufficient for an accurate calculation of the far-field. The PWE of the same electric field $\bar{E}$ in the spectral k_xk_y-domain valid for $z > z_o$ is given by [4],

$$\bar{E}(x,y,z) = \frac{1}{2\pi} \int_{-\infty}^{\infty} \int_{-\infty}^{\infty} \bar{T}(k_x,k_y) e^{ik_z z} e^{i(k_x x + k_y y)} dk_x dk_y \tag{2}$$

where k_x and k_y, are the spectral variables and $k_z = \sqrt{k^2 - k_x^2 - k_y^2}$. The plane wave spectrum for a given z-coordinate is $\bar{T}(k_x,k_y,z) \equiv \bar{T}(k_x,k_y)e^{ik_z z}$. The spectral domain is divided into two regions, the visible region, for $k_x^2 + k_y^2 \le k^2$, which contains the propagating plane waves, and the invisible region, for $k_x^2 + k_y^2 > k^2$, which contains the evanescent plane waves, see Fig. 3. The two variables k_x and k_y are real, while k_z is real in the visible region but purely imaginary with a positive imaginary part in the invisible region. In practice, the k_x- and k_y-integrals are truncated at finite values $\pm k_{xmax}$ and $\pm k_{ymax}$ respectively, providing a spatial resolution (δ_x, δ_y) in the aperture field equal to $\delta_x = \pi / k_{xmax}$, $\delta_y = \pi / k_{ymax}$. At the border between the visible and invisible regions $k_z = 0$ and the PWE generally possesses a singularity there [4].

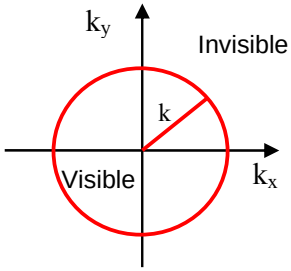

Figure 3. Visible and invisible regions of the spectral k_xk_y-domain.

It can be shown [1][2] that the SWE of Eq. 1 can be rigorously transformed into the PWE of Eq. 2, if the plane wave spectrum $\bar{T}(k_x,k_y,z)$ is written as

$$\bar{T}(k_x,k_y,z) = \sum_{n=1}^{\infty} \sum_{m=-n}^{n} Q_{1mn}^{(3)} \bar{T}_{1mn}(k_x,k_y,z) + Q_{2mn}^{(3)} \bar{T}_{2mn}(k_x,k_y,z) \tag{3}$$

where

$$\bar{T}_{1mn}(k_x,k_y,z)=\frac{e^{ik_z z}}{k_z}\frac{(-i)^{n+1}}{\sqrt{\eta}\sqrt{n(n+1)}}\bar{Y}_n^m(\alpha,\beta) \quad (4)$$

$$\bar{T}_{2mn}(k_x,k_y,z)=\frac{e^{ik_z z}}{k_z}\frac{(-i)^{n}}{\sqrt{\eta}\sqrt{n(n+1)}}\hat{k}\times\bar{Y}_n^m(\alpha,\beta) \quad (5)$$

with $\hat{k}=\bar{k}/k=(k_x\hat{x}+k_y\hat{y}+k_z\hat{z})/k$. The function $\bar{Y}_n^m(\alpha,\beta)$ is the vector spherical harmonics [1], with $\alpha\in$ B, see Fig. 4, equal to $\alpha=\text{acos}(k_z/k)$, and $\beta\in[-\pi,\ \pi]$ and equal to $\beta=\text{atan}(k_y/k_x)$. Eq. 3 shows that the plane wave spectrum on any z-plane $z > z_o$ can be expressed as a series of the same type and with the same Q coefficients of the SWE of Eq. 1, where the basis functions are now the vector spherical harmonics. The imaginary values of the angle α correspond to the invisible region of the k_xk_y-domain. Though the functions $\bar{Y}_n^m(\alpha,\beta)$ have an exponential growth in that region, it is important to note that the series of Eq. 3 is convergent in the entire spectral domain.

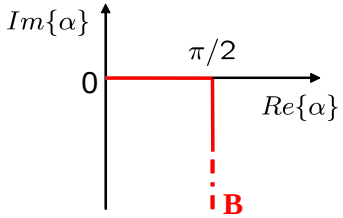

Figure 4. Domain of the variable α on contour B.

Nevertheless, while the visible region of the spectrum reaches convergence with $N \approx kr_o$ terms, the invisible generally requires many more terms to compensate the exponential growth of the spherical harmonics [1][2]. In practice, the finite dynamic range of the measurement system limits the measurement of these high order modes. However, it has been shown [1] that the recovery of the visible region and the singularity for $k_z = 0$, both correctly represented by the first $N \approx kr_o$ modes, provides accurate aperture fields that facilitate an effective diagnostics.

3 Faulty elements and diagnostics results

During the final calibration measurements of the MIRAS, see Figs. 1 and 5, anomalies were discovered in the far-field patterns of two receivers:

1) Port 1 of the receiver unit BC03 showed a high cross-polarisation in the $\varphi = 90°$ plane.

2) Port 1 of the receiver unit A05 exhibited a noticeable frequency variation in all φ planes.

In order to identify the sources of those anomalies, the SWE-to-PWE diagnostics technique was applied and the aperture fields for these two receivers were computed on the z-plane placed on the surface of the Kapton-Germanium protection layer, see Fig. 1, located at z = -5mm in the measurement coordinate system. For reference, the diagnostics was also applied to the unit A01 (port 1) which did not present any anomalies. Its co- and cross-polar far-field patterns (Ludwig 3rd definition [3]) are shown in Fig. 6 for $\varphi = 90°$.

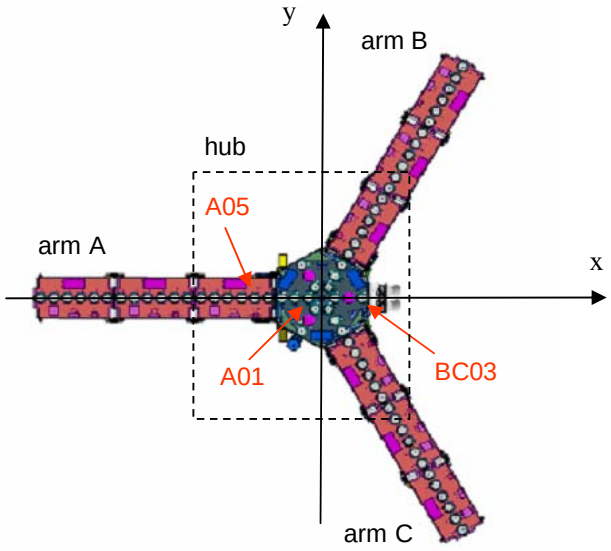

Figure 5. The MIRAS antenna system in the measurement coordinate system with the faulty units A05 and BC03 and the correct unit A01 indicated.

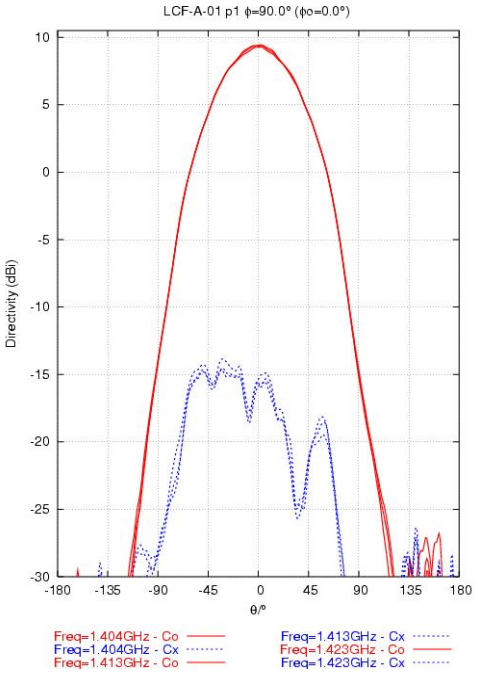

Figure 6. Far-field pattern of the receiver unit A01, port 1, for $\varphi = 90°$, showing correct co- and cross-polar components.

3.1 Element BC03

The far-field pattern of port 1 of the receiver unit BC03 in the $\varphi = 90°$ plane is shown in Fig. 7: it exhibits a correct co-polar

component, but an unusual high cross-polar level at all frequencies of interest when compared to the reference pattern of Fig. 6.

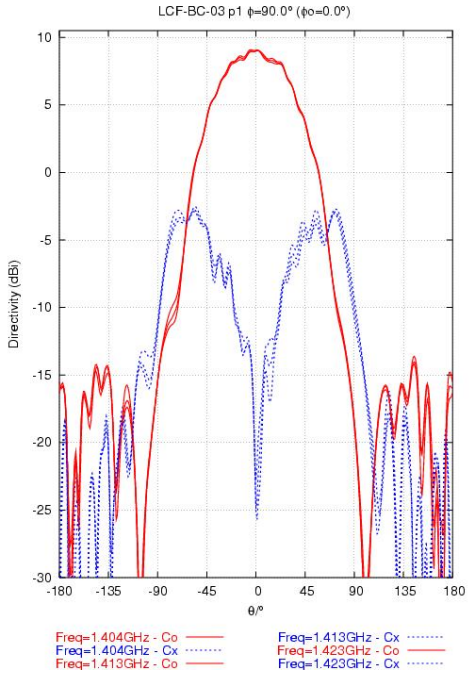

Figure 7. Far-field pattern of the receiver unit BC03, port 1, for $\varphi = 90°$, showing an unusual high cross-polar component.

From the Q coefficients of the SWE the power spectrum $P_{rad}(n) = \frac{1}{2}\sum_{m=-n}^{n}\left|Q_{1mn}^{(3)}\right|^2 + \left|Q_{2mn}^{(3)}\right|^2$ has been found, see Fig. 8.

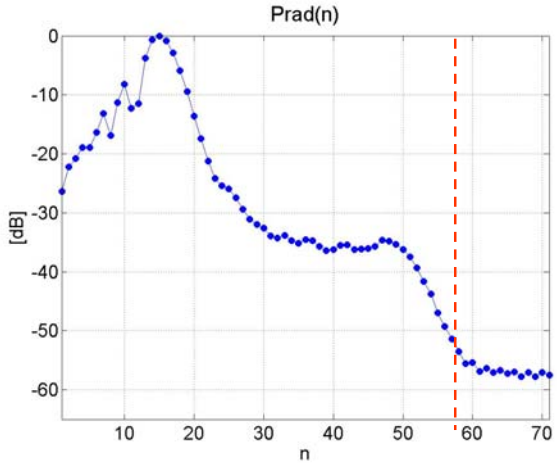

Figure 8. Power spectrum of the unit BC03 at f =1.423GHz, and the truncation value N = 58.

It is seen that the finite dynamic range of the measurement system allows the correct acquisition of N = 58 modes which, at a frequency f =1.423 GHz and with r_o being equal to 9λ, corresponds to $N = 58 = kr_o+2$. With this n-truncation in the series of Eq. 3 it is expected to recover only the visible part of the plane wave spectrum and the singularity at k_z = 0. A calculation of the invisible region to improve the spatial resolution of the aperture fields is not possible due to an insufficient number of n-modes. The plane wave spectrum $\overline{T}(k_x, k_y, z)$ has thus been calculated with Eq. 3, see Fig. 9 for a plot of the y-component in dB scale on the [-2k, 2k] spectral domain. It is possible to notice the recovery of the visible region and the singularity at $k_z = 0$, while it is evident that the convergence of points belonging to the invisible region is not reached yet. The invisible region is thus replaced by zeros and the spectrum is then inverse Fourier transformed to obtain the aperture field.

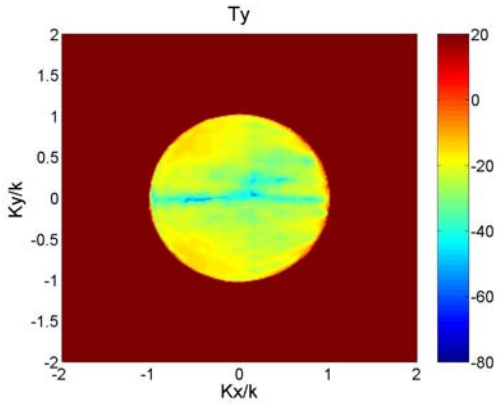

Figure 9. Amplitude of T_y, unit BC03, in dB on z = -5mm with N = 58: the visible region and the singularity are reconstructed, while the convergence in the invisible region is not reached for this value of N.

In Fig. 10 the amplitudes of the cross-polar components E_y and E_z are plotted in dB. It is possible to distinguish the radiation from the circular patch as well as the diffraction from the edges of the hub. Moreover, for both components the radiation from the patch shows asymmetries with respect to the axis parallel to the y-axis and passing through the center of the patch. It was thus concluded that the anomalies of the pattern in Fig. 7 were due to an error in the patch excitation, i.e., in the patch feed network. The unit BC03 was subsequently replaced by a new one and, after a new spherical near-field measurement, the aperture fields were calculated, see Fig. 11. It is noted that the patch excitation is now totally symmetric and the diffraction from the edges has decreased slightly with respect to the faulty element case shown in Fig. 10.

The circular ripples in the near-fields shown in Figs. 10 and 11 are artefacts caused by the truncation of the plane wave spectrum at the border of the visible region. This is the general consequence of a convolution with a sinc function in the transformed spatial domain. For high directive antennas, i.e., when the plane wave spectrum is highly concentrated inside the visible region and has low values at the border of the visible region, this ripple effect is negligible. For low directive antennas, i.e., when the plane wave spectrum is distributed on the entire visible region, this ripple effect becomes evident. The artefact can however be reduced by use of windowing prior to Fourier transform; to this end a

multitude of well-established signal processing techniques is available [9].

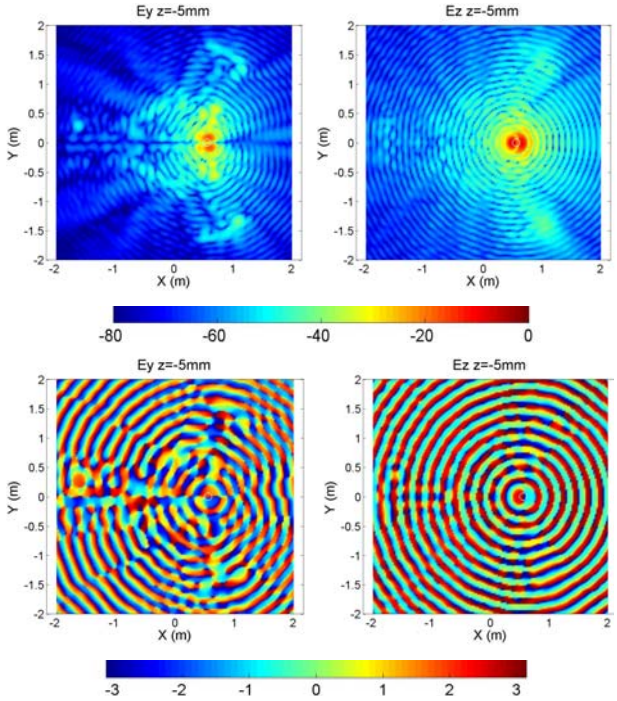

Figure 10. Amplitude in dB and phase in radians of E_y and E_z, unit BC03, on $z = -5$mm .

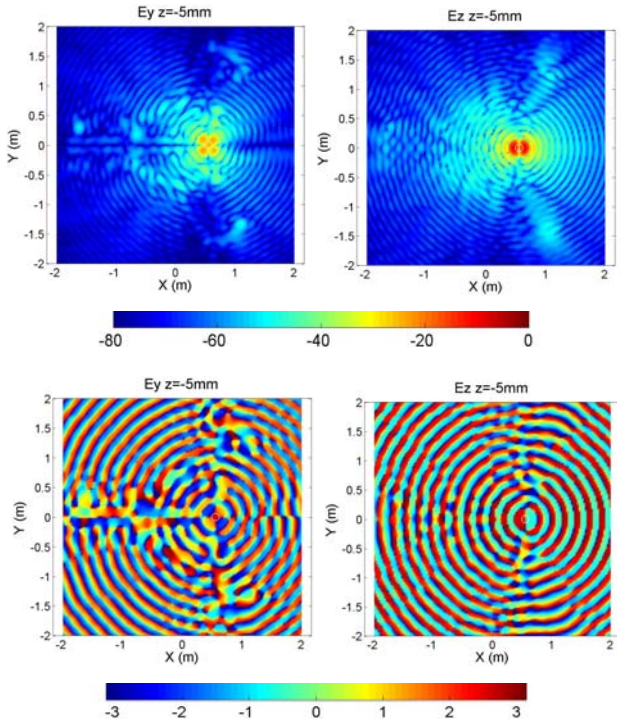

Figure 11. Amplitude in dB and phase in radians of E_y and E_z, unit BC03 replaced, on $z = -5$mm .

3.2 Element A05

The far-field pattern of port 1 of the receiver unit A05 in the $\varphi = 0°$ plane is shown in Fig. 12: the co-polar component clearly shows an unusual frequency variation.

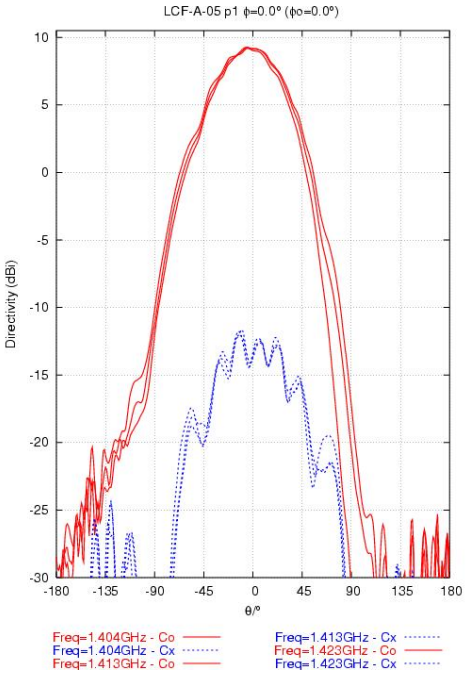

Figure 12. Far-field pattern of the receiver unit A05, port 1, for $\varphi = 0°$, showing an unusually large frequency variation.

This anomaly was observed in all φ planes and in some of them also for the cross-polar component. In order to highlight and isolate the effect of the frequency variation, the diagnostics was also applied to the correct element A01. From the measured Q coefficients the power spectrum was computed and it was found that again a truncation of the n-modes at $N = 58$ was necessary for both elements. Following the same procedure used for the unit BC03, the spectra were computed on the [-2k, 2k] spectral domain with the use of the SWE-to-PWE transformation of Eq. 3 on the z-plane $z = -5$mm , and then inverse Fourier transformed. Again, for both units only the visible region and the singularity for $k_z = 0$ were recovered, while the entire invisible region did not reach the convergence with $N = 58$ and was thus replaced by zeros.

In Fig. 13 the y-component of the aperture field of the faulty unit A05 is compared to the corresponding component of the correct unit A01 for the three frequencies of interest, f=1.404 GHz, 1.413 GHz and 1.423GHz. While the behaviour of the unit A01 remains constant with frequency, the unit A05 shows significant changes. In particular it is noticed that the field at the antenna itself is asymmetric and changes with frequency; furthermore, the diffraction from the hub edges decreases with increasing frequency. The same happens to the z-component, while it becomes less evident for the co-polar x-component. The same asymmetries were noticed also in the phase plots. Again, it was concluded that the anomalies

detected in the far-field pattern were due to errors in the feed network.

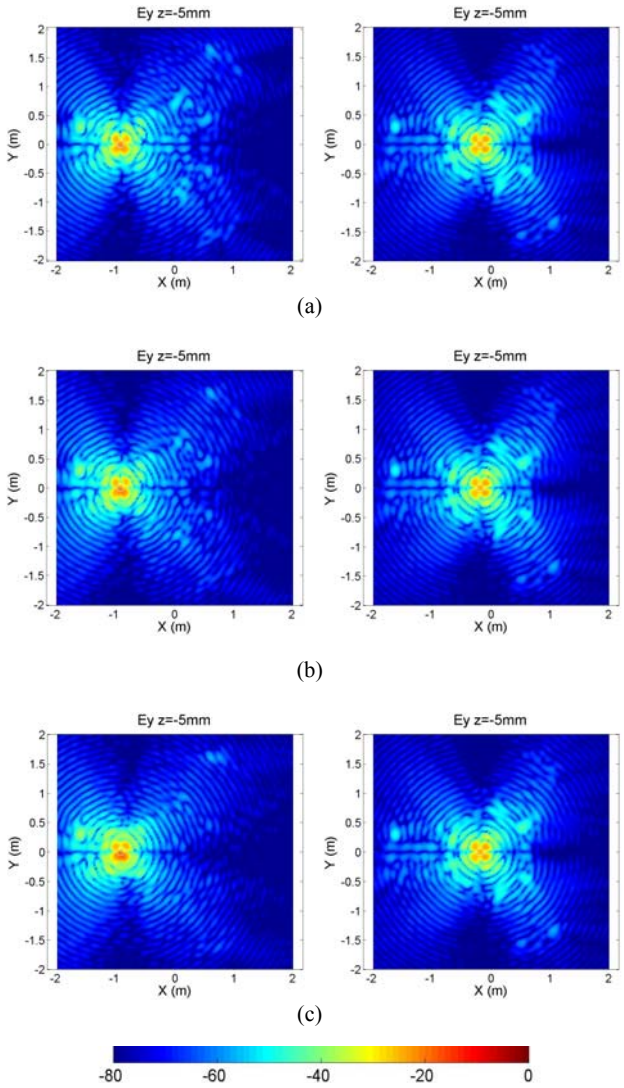

Figure 13. Amplitude of E_y in dB on the z-plane z = -5mm: on the left the unit A05 (faulty) on the right the unit A01 (correct): (a) f=1.404GHz (b) f=1.413GHz (c) f=1.423GHz.

4 Conclusions

A diagnostics of two units of the SMOS MIRAS antenna system has been performed by applying the SWE-to-PWE antenna diagnostics technique to the measurements of the final on-ground calibration at the DTU-ESA Spherical Near-Field Antenna Test Facility. The diagnostics showed that the anomalies observed in the far-field pattern could be traced back to asymmetries and frequency variations in the extreme near-field of the two antenna elements. In both cases, it was concluded that errors were present in the feed networks of the units, for port 1 only, and the presence of such errors was later confirmed by an inspection of the antenna hardware. It is noticed, that the calculated aperture fields show not only the field radiated directly by the antenna unit but also quite clearly the diffraction from the edges and other structural components of the support structure.

The investigation presented here also serves as an experimental validation of the SWE-to-PWE antenna diagnostics technique in presence of typical measurement inaccuracies and highlights the importance of the analysis of the cross-polar components, in amplitude as well as in phase, for the purpose of antenna diagnostics.

References

[1] C. Cappellin, A. Frandsen, O. Breinbjerg. "On the relationship between the Spherical Wave Expansion and the Plane Wave Expansion", AMTA Europe Symposium, Munich, Germany, 2006.

[2] C. Cappellin, O. Breinbjerg, A. Frandsen. "The influence of finite measurement accuracy on the SWE-to-PWE antenna diagnostics technique", EuCap European Conference on Antennas and Propagation, Nice, France, 2006.

[3] J.E. Hansen. "Spherical Near-Field Antenna Measurements", Peter Peregrinus Ltd. London, 1988.

[4] T.B. Hansen, A.D. Yaghjian. "Plane Wave Theory of Time-Domain Fields, Near-Field Scanning Applications", IEEE PRESS, 1999.

[5] Homepage of the SMOS mission: http://www.esa.int/esaLP/LPsmos.html.

[6] Homepage of the DTU-ESA Facility: http://www.oersted.dtu.dk/English/research/emi/afg/dtu_esa_facility.aspx.

[7] S. Pivnenko, J. M. Nielsen, O. Breinbjerg. "Aspects of antenna pattern characterization of an L-band space radiometer", AMTA 2003, Irvine, California, 2003, 375-379.

[8] S. Pivnenko, J. M. Nielsen, O. Kim, O. Breinbjerg. "SMOS antenna measurements. Phase C/D investigatory measurements", Report. No: SO-TR-DTU-ANT-0004, 2 volumes, Technical University of Denmark, Ørsted-DTU, EMI, October 2005 (R 725).

[9] H. C. Stanwitz, R. J. Dallaire, J. R. Fienup. "Nonlinear apodization for sidelobe control in SAR imagery", *IEEE Trans. on Aer. and Elect. Syst.*, vol. 31, no. 1, 267-279, Jan 1995.